

Exploiting High-order Phase-shift Keying Modulation and Direct-detection in Silicon Photonic Systems

JIE YOU¹ AND NICOLAE C. PANOIU^{1,*}

¹*Department of Electronic and Electrical Engineering, University College London, Torrington Place, London WC1E 7JE, United Kingdom*

*n.panoiu@ucl.ac.uk

Abstract: A computational approach to evaluate the bit-error ratio (BER) in silicon photonic systems employing high-order phase-shift keying (PSK) modulation formats is presented. Specifically, the investigated systems contain a silicon based optical interconnect, namely a strip silicon photonic waveguide or a silicon photonic crystal waveguide, and direct-detection receivers suitable to detect PSK and amplitude-shaped PSK signals. The superposition of a PSK signal and complex additive white Gaussian noise passes through the optical interconnect and subsequently through two detection-branch receivers. To model the signal propagation in the silicon optical interconnects we used a modified nonlinear Schrödinger equation, which incorporates all relevant linear and nonlinear optical effects and the mutual interaction between free-carriers and the optical field. Finally, the BER is calculated by applying a frequency-domain approach based on the Karhunen-Loève series expansion method. Our computational studies of the BER reveal that the optical power, type of PSK modulation, waveguide length, and group-velocity are key factors characterizing the system BER, their influence on BER being more significant in a photonic system with larger nonlinearity. In particular, our analysis shows that the system performance is affected to a much larger extent when the signal propagates in the slow-light regime, despite the fact that this regime allows for a significantly reduced length of optical interconnects.

© 2017 Optical Society of America

OCIS codes: (200.4650) Optical interconnects; (070.4340) Nonlinear optical signal processing; (130.3120) Integrated optics devices; (230.7370) Waveguides; (130.5296) Photonic crystal waveguides; (060.4510) Optical communications.

References and links

1. F. Benner, M. Ignatowski, J. A. Kash, D. M. Kuchta, and M. B. Ritter, "Exploitation of optical interconnects in future server architectures," *IBM J. Res. Dev.* **49**, 755–775 (2005).
2. K. Shacham, K. Bergman, and L. P. Carloni, "Photonic networks-on-chip for future generations of chip multiprocessors," *IEEE Trans. Comput.* **57**, 1246–1260 (2008).
3. J. A. Kash, A. F. Benner, F. E. Doany, D. M. Kuchta, B. G. Lee, P. K. Pepeljugoski, L. Schares, C. L. Schow, and M. Taubenblatt, "Optical Interconnects in Exascale Supercomputers," *23rd Annual Meeting of the IEEE Photonics Society*, 483–484 (2010).
4. R. Ho, K. W. Mai, and M. A. Horowitz, "The future of wires," *Proc. IEEE* **89**, 490–504 (2001).
5. C. Gunn, "CMOS Photonics for High-Speed Interconnects," *IEEE Micro* **26**, 58–66 (2006).
6. Y. A. Vlasov, "Si CMOS-Integrated Nano-Photonics for Computer and Data Communications Beyond 100G," *IEEE Commun. Mag.* **50**, S67–S72 (2012).
7. W. Bogaerts, R. Baets, P. Dumon, V. Wiaux, S. Beckx, D. Taillaert, B. Luyssaert, J. van Campenhout, P. Bienstman, and D. van Thourhout, "Nanophotonic waveguides in silicon-on-insulator fabricated with CMOS technology," *J. Lightwave Technol.* **23**, 401–412 (2005).
8. T. Barwicz, H. Byun, and F. Gan, C. W. Holzwarth, M. A. Popovic, P. T. Rakich, M. R. Watts, E. P. Ippen, F. X. Kartner, H. I. Smith, J. S. Orcutt, R. J. Ram, V. Stojanovic, O. O. Olubuyide, J. L. Hoyt, S. Spector, M. Geis, M. Grein, T. Lyszczarz, and J. U. Yoon, "Silicon photonics for compact, energy-efficient interconnects," *J. Opt. Netw.* **6**, 63–73 (2007).
9. K. K. Lee, D. R. Lim, H. C. Luan, A. Agarwal, J. Foresi, and L. C. Kimerling, "Effect of size and roughness on light transmission in a Si/SiO₂ waveguide: Experiments and model," *Appl. Phys. Lett.* **77**, 1617–1619 (2000).
10. R. U. Ahmad, F. Pizzuto, G. S. Camarda, R. L. Espinola, H. Rao, and R. M. Osgood, "Ultracompact corner-mirrors and T-branches in silicon-on-insulator," *IEEE Photon. Technol. Lett.* **14**, 65–67 (2002).
11. X. Chen, N. C. Panoiu, and R. M. Osgood, "Theory of Raman-mediated pulsed amplification in silicon-wire waveguides," *IEEE J. Quantum Electron.* **42**, 160–170 (2006).

12. A. C. Turner, C. Manolatou, B. S. Schmidt, M. Lipson, M. A. Foster, J. E. Sharping, and A. L. Gaeta, "Tailored anomalous group-velocity dispersion in silicon channel waveguides," *Opt. Express* **14**, 4357–4362 (2006).
13. R. A. Soref and B. R. Bennett, "Electrooptical effects in silicon," *IEEE J. Quantum Electron.* **23**, 123–129 (1987).
14. A. Liu, R. Jones, L. Liao, D. Samara-Rubio, D. Rubin, O. Cohen, R. Nicolaescu, and M. Paniccia, "A high-speed silicon optical modulator based on a metal-oxide-semiconductor capacitor," *Nature* **427**, 615–618 (2004).
15. Q. Xu, B. Shmidt, S. Pradhan, and M. Lipson, "Micrometre-scale silicon electro-optic modulator," *Nature* **435**, 325–327 (2005).
16. R. Claps, D. Dimitropoulos, V. Raghunathan, Y. Han, and B. Jalali, "Observation of stimulated Raman amplification in silicon waveguides," *Opt. Express* **11**, 1731–1739 (2003).
17. H. S. Rong, R. Jones, A. S. Liu, O. Cohen, D. Hak, A. Fang, and M. Paniccia, "A continuous-wave Raman silicon laser," *Nature* **433**, 725–728 (2005).
18. O. Boyraz, P. Koonath, V. Raghunathan, and B. Jalali, "All optical switching and continuum generation in silicon waveguides," *Opt. Express* **12**, 4094–4102 (2004).
19. H. Fukuda, K. Yamada, T. Shoji, M. Takahashi, t. Tsuchizawa, T. Watanabe, J. Takahashi, and S. Itabashi, "Four-wave mixing in silicon wire waveguides," *Opt. Express* **13**, 4629–4637 (2005).
20. M. A. Foster, A. C. Turner, J. E. Sharping, B. S. Schmidt, M. Lipson, and A. L. Gaeta, "Broad-band optical parametric gain on a silicon photonic chip," *Nature* **441**, 960–963 (2006).
21. E. Dulkeith, Y. A. Vlasov, X. Chen, N. C. Panoiu, and R. M. Osgood, "Self-phase-modulation in submicron silicon-on-insulator photonic wires," *Opt. Express* **14**, 5524–5534 (2006).
22. N. C. Panoiu, X. Chen, and R. M. Osgood, "Modulation instability in silicon photonic nanowires," *Opt. Lett.* **31**, 3609–3611 (2006).
23. I-W. Hsieh, X. Chen, J. I. Dadap, N. C. Panoiu, R. M. Osgood, S. J. McNab, and Y. A. Vlasov, "Crossphase modulation-induced spectral and temporal effects on co-propagating femtosecond pulses in silicon photonic wires," *Opt. Express* **15**, 1135–1146 (2007).
24. R. Dekker, A. Driessen, T. Wahlbrink, C. Moormann, J. Niehusmann, and M. Forst, "Ultrafast Kerr-induced alloptical wavelength conversion in silicon waveguides using 1.5 μm femtosecond pulses," *Opt. Express* **14**, 8336–8346 (2006).
25. S. Assefa, F. Xia, W. M. J. Green, C. L. Schow, A. V. Rylyakov, and Y. A. Vlasov, "CMOS-Integrated Optical Receivers for On-Chip Interconnects," *IEEE J. Sel. Top. Quantum Electron.* **16**, 1376–1385 (2010).
26. N. C. Panoiu, X. Liu, and R. M. Osgood, "Self-steepening of ultrashort pulses in silicon photonic nanowires," *Opt. Lett.* **34**, 947–949 (2009).
27. R. A. Soref, "The past, present, and future of silicon photonics," *IEEE J. Sel. Top. Quantum Electron.* **12**, 1678–1687 (2006).
28. Q. Lin, O. J. Painter, and G. P. Agrawal, "Nonlinear optical phenomena in silicon waveguides: Modeling and applications," *Opt. Express* **15**, 16604–16644 (2007).
29. J. I. Dadap, N. C. Panoiu, X. G. Chen, I. W. Hsieh, X. P. Liu, C. Y. Chou, E., Dulkeith, S. J., McNab, F. N. Xia, W. M. J. Green, L. Sekaric, Y. A. Vlasov, and R. M. Osgood, "Nonlinear-optical phase modification in dispersion-engineered Si photonic wires," *Opt. Express* **16**, 1280–1299 (2008).
30. R. M. Osgood, N. C. Panoiu, J. I. Dadap, X. Liu, X. Chen, I-W. Hsieh, E. Dulkeith, W. M. J. Green, and Y. A. Vlasov, "Engineering nonlinearities in nanoscale optical systems: physics and applications in dispersion-engineered silicon nanophotonic wires," *Adv. Opt. Photon.* **1**, 162–235 (2009).
31. J. P. Winzer and R. J. Essiambre, "Advanced optical modulation formats," *Proc. IEEE* **94**, 952–985 (2006).
32. M. Rohde, C. Caspar, N. Heimes, M. Konitzer, E. J. Bachus, and N. Hanik, "Robustness of DPSK direct detection transmission format in standard fibre WDM systems," *Electron. Lett.* **36**, 1483–1484 (2000).
33. J. Wang and J. M. Kahn, "Impact of Chromatic and Polarization-Mode Dispersions on DPSK Systems Using Interferometric Demodulation and Direct Detection," *J. Lightwave Technol.* **22**, 362–371 (2004).
34. M. Seimetz, M. Nolle, and E. Patzak, "Optical System With High-Order Optical DPSK and Star QAM Modulation Based on Interferometric Direct Detection," *J. Lightwave Technol.* **25**, 1515–1530 (2007).
35. M. Nolle, M. Seimetz, and E. Patzak, "System Performance of High-Order Optical DPSK and Star QAM Modulation for Direct Detection Analyzed by Semi-Analytical BER Estimation," *J. Lightwave Technol.* **27**, 4319–4329 (2009).
36. N. C. Panoiu, J. F. McMillan, and C. W. Wong, "Theoretical Analysis of Pulse Dynamics in Silicon Photonic Crystal Wire Waveguides," *IEEE J. Sel. Top. Quantum Electron.* **16**, 257–266 (2010).
37. S. Lavdas and N. C. Panoiu, "Theory of pulsed four-wave mixing in one-dimensional silicon photonic crystal slab waveguides," *Phys. Rev. B* **93**, 115435 (2016).
38. C. Koos, L. Jacome, C. Poulton, J. Leuthold, W. Freude, "Nonlinear silicon-on-insulator waveguides for all-optical signal processing," *Opt. Express* **15**, 5976–5990 (2007).
39. A. Mafi and S. Raghavan, "Nonlinear phase noise in optical communication systems using eigenfunction expansion method," *Opt. Eng.* **50**, 055003 (2011).
40. E. Forestieri and M. Secondini, "On the Error Probability Evaluation in Lightwave Systems With Optical Amplification," *J. Lightwave Technol.* **27**, 706–717 (2009).
41. J. You, S. Lavdas, and N. C. Panoiu, "Theoretical Comparative Analysis of BER in Multi-Channel Systems With Strip and Photonic Crystal Silicon Waveguides," *IEEE J. Sel. Top. Quantum Electron.* **22**, 4400810 (2016).
42. J. You and N. C. Panoiu, "Calculation of Bit Error Rates in Optical Systems with Silicon Photonic Wires," *IEEE J. Quantum Electron.* **51**, 8400108 (2015).

43. P. E. Barclay, K. Srinivasan, and O. Painter, "Nonlinear response of silicon photonic crystal microresonators excited via an integrated waveguide and fiber taper," *Opt. Express* **13**, 801–820 (2005).
 44. H. Yoon, D. Lee, and N. Park, "Performance comparison of optical 8-ary differential phase-shift keying systems with different decision schemes," *Opt. Express* **13**, 371–376 (2005).
 45. E. Agrell and M. Karlsson, "Performance comparison of optical 8-ary differential phase-shift keying systems with different decision schemes: Comment," *Opt. Express* **14**, 1700–1701 (2006).
-

1. Introduction

Rapidly increasing needs for large data transfer in optical networks with decreasing footprint, driven by cloud data centers and the push to develop next generation, exaflop supercomputers, in connection with a growing role of photonics in on-chip interconnect infrastructure for chip multiprocessors architectures, have been leading to an increasing role of optical communications in rack-to-rack and board-to-board communication systems. In this context, optical interconnects [1–3] are viewed as an increasingly appealing alternative to copper wires [4], particularly due to their high capacity, ultra-broadband transparency window, and fundamentally low energy consumption. Equally important, recent progress in nanofabrication technologies and advances in photonic device integration at the chip scale [5, 6], allow photonics to become ever more pervasive in chip-level communications networks.

One of the most successful approaches to seamlessly integrate photonics into chip-level networks is provided by the silicon-on-insulator (SOI) material platform. In addition to its compatibility with the CMOS fabrication processing technologies [7, 8], SOI platform provides a series of advantages stemming directly from its structure and optical properties of the constituent materials. Thus, the high-index contrast between silicon (Si, $n_{\text{Si}} \approx 3.46$) and buried-oxide substrate ($n_{\text{SiO}_2} \approx 1.45$) and cladding (air, $n_{\text{air}} = 1$) makes it possible to tightly confine and guide light using ultracompact optical waveguides with deep-subwavelength transverse dimensions [9, 10]. This strong light confinement enables another key functionality of these optical interconnects, namely the possibility to greatly engineer their dispersion properties [11, 12], either by changing the dimensions of the Si photonic waveguide (Si-PhW) or by patterning them as is the case with Si photonic crystal (PhC) waveguides (Si-PhCWs). These latter structures allows one to dramatically change the propagation regime of the optical signal, e.g. from fast-light (FL) to slow-light (SL) regime. Moreover, the dependence of the index of refraction of silicon on the carrier density facilitates ultrafast modulation and active control of light propagation in such waveguides [13–15]. Equally important, silicon possesses very large third-order optical nonlinearities in a broad spectral range, which means that key active optical functionalities, such as Raman amplification, self- and cross-phase modulation, four-wave mixing, and pulse self-steepening can be easily implemented using this optical material. In particular, these functionalities and active devices based on these nonlinear optical processes have been demonstrated [16–26] (see [27–30] for a review of silicon photonics and related device applications).

The performance of optical communication networks can be improved not only at the device layer but also by using advanced optical processing techniques. In particular, advanced optical modulation formats have been intensively investigated over the recent years [31], as they can potentially become viable alternatives to more commonly used ON-OFF keying (OOK) modulation. In the context of optical fiber communications it has become clear that, among the advanced modulation formats of optical signals, phase-shift keying (PSK) modulation provides unique advantages, including increased spectral efficiency, superior tolerance to chromatic dispersion and polarization-mode dispersion, and less stringent bandwidth requirements [32, 33]. Moreover, higher spectral efficiency can be achieved by employing PSK modulation schemes with increased complexity, such as quadrature PSK (4PSK) and 8-ary PSK (8PSK) modulation formats, or by combining amplitude-shift keying (ASK) and PSK formats, which we call here ASK-PSK modulation schemes. Importantly, whereas high-order modulation formats have been studied

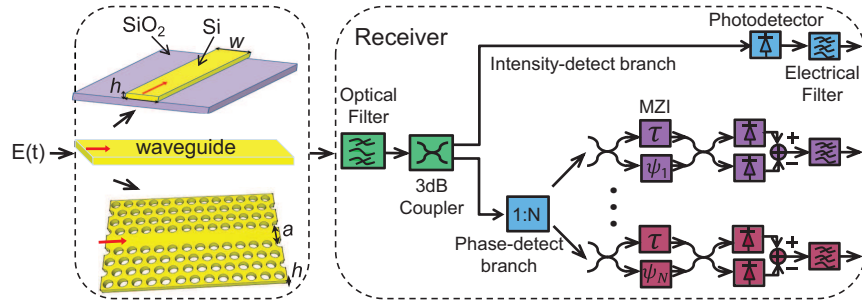


Fig. 1. Schematics of the Si photonic system investigated in this work. It contains a Si waveguide and a direct-detection receiver with bi-level electrical decisions. The receiver has two branches, an intensity-detection and a phase-detection branch, with the latter consisting of N Mach-Zehnder interferometers. Two types of waveguides are investigated: one is a strip waveguide with uniform cross-section with height, $h = 250$ nm, and width, $w = 900$ nm and the other one is a PhC waveguide with lattice constant, $a = 412$ nm, hole radius, $r = 0.22a$, and slab thickness, $h = 0.6a$.

extensively in the context of optical fiber and other communication systems [31, 34, 35], currently a similar theoretical analysis addressing the performance of such modulation schemes when used in photonics systems containing silicon based optical communication links is not available.

In this paper, we study theoretically the performance of photonic systems containing single-channel Si-PhWs or Si-PhCWs and utilizing PSK, OOK, and ASK-PSK modulated signals. The system investigated in this work consists of a single-mode Si-PhW or Si-PhCW, the latter being operated either in the FL or SL regime, linked to a direct-detection receiver containing an intensity-detect branch and phase-detect branch (see Fig. 1). The system dynamics was described by a modified nonlinear Schrödinger equation governing the propagation of the optical field coupled to a standard rate equation describing the evolution of free-carriers (FCs) [11, 30, 36–38]. Moreover, the statistical properties of the transmitted signal were analyzed using the frequency-domain Karhunen-Loève (KL) method [39, 40]. This analysis was performed for different values of key system parameters and for several modulation formats.

The paper is organized as follows. In Sec. 2, we introduce the models that govern the propagation of the noisy signal in the Si waveguides. Then, in Sec. 3, we describe the advanced modulation formats and the details of direct-detection receivers considered in this work. This is followed by the description of the bit-error ratio (BER) calculation method, which is presented in Sec. 4. These theoretical and computational tools are used in Sec. 5 to analyze the system performance corresponding to several modulation formats, for different values of the main system parameters. Finally, the main results are summarized in the last section.

2. Theory of Propagation of Optical Signals in Silicon Waveguides

In this section, we introduce a rigorous theoretical model describing the coupled dynamics of the optical field and FCs in the two types of Si waveguides investigated in this work. In our analysis, we assume that the input optical field consists of a superposition between the PSK signal and complex additive white Gaussian noise (AWGN), the mutual interaction between the optical signal and noise being mediated by FCs and nonlinear optical effects. In order to reduce the computational time, we also use a linearized model of the full propagation model, derived here in the vanishingly small noise limit.

2.1. Full Theoretical Model

The slowly varying complex envelope of the electrical field of the input PSK optical signal and the complex AWGN are written as $s(z = 0, t)$ and $a(z = 0, t)$, respectively, the total input optical field being $u(z = 0, t) = s(z = 0, t) + a(z = 0, t)$. Here, z and t are the distance along the waveguide and time, respectively. Mathematically, the full propagation model can be written as follows [11, 30, 36, 37]:

$$i \frac{\partial u(z, t)}{\partial z} - \frac{\beta_2}{2} \frac{\partial^2 u}{\partial t^2} + \frac{ic\kappa}{2nv_g} (\alpha_i + \alpha_{fc}) u(z, t) + \frac{\omega_0 \kappa}{nv_g} \delta n_{fc} u(z, t) + \gamma |u(z, t)|^2 u(z, t) = 0, \quad (1)$$

$$\frac{\partial N}{\partial t} = -\frac{N}{t_c} + \frac{\gamma''}{\hbar\omega_0 A_{nl}} |u(z, t)|^4, \quad (2)$$

where $N(z, t)$ is the FC density, β_2 is the second-order dispersion coefficient, κ accounts for the overlap between the optical mode and the waveguide active area, v_g is the group-velocity (GV), t_c is the FC relaxation time, α_i is the intrinsic loss coefficient, δn_{fc} and α_{fc} are the FC-induced refractive index change and FC loss coefficient, respectively, and A_{nl} is the effective mode area. We use $A_{nl} = wh$ ($A_{nl} = ah$) for the Si-PhW (Si-PhCW) systems, although more accurate formulae for A_{nl} exist [30, 36–38]. Since we consider high-index contrast systems, the optical field is strongly confined in the waveguide, so that using the geometrical area for A_{nl} is a reasonable approximation. In this paper, the symbols “’” and “''” stand for the real and imaginary parts of a complex quantity, respectively. Moreover, the nonlinear waveguide coefficient, γ , is given by:

$$\gamma = \begin{cases} \frac{3\omega_0 \epsilon_0}{16v_g^2} \frac{\Gamma}{\mathcal{W}^2}, & \text{for Si - PhWs,} \\ \frac{3\omega_0 \epsilon_0 a}{16v_g^2} \frac{\Gamma}{W^2}, & \text{for Si - PhCWs,} \end{cases} \quad (3)$$

where Γ is the effective third-order susceptibility of the optical mode, \mathcal{W} is the optical energy per unit length of the mode of the Si-PhW, and W is the optical energy of the optical mode contained in a unit cell with length, a , of the Si-PhCW.

In our analysis, we decompose the optical field propagating in the Si waveguide into a signal part and noise:

$$u(z, t) = [\sqrt{P(z)} e^{i\Phi_0} + a(z, t)] e^{-i\Phi(z)}, \quad (4)$$

where $P(z)$ is the power of the continuous-wave (CW) PSK signal, Φ_0 is the phase of the PSK signal, and $\Phi(z)$ is a global phase shift, whose value depends on the signal modulation format and waveguide properties. For m -ary PSK (m PSK), $\Phi_0 = 2(n-1)\pi/m$, where $n = 1, 2, \dots, m$. In the case of ASK-PSK signals, the phases Φ_0 are the same but the signal power P can have several values; the OOK is the particular case defined by $\Phi_0 = 0$.

In the stationary regime $\frac{\partial N}{\partial t} = 0$, so that the steady state FC density, N_s , is given by:

$$N_s(z) = \frac{\gamma'' t_c}{\hbar\omega_0 A_{nl}} P^2(z) \equiv \xi P^2(z). \quad (5)$$

A self-consistency condition for the validity of our model is that the FC induced dispersion is small, namely $\delta n_{fc} \lesssim 10^{-3}$. In addition, stationary regime can be reached only if the bit window is much smaller than the FC relaxation time, a condition satisfied in all our numerical simulations.

2.2. Linearized Theoretical Model

In the small noise limit, Eqs. (1)–(2) can be linearized and transformed to a system of ordinary differential equations (ODEs), which is much less demanding computationally. Thus, by substituting Eq. (4) into Eq. (1) and keeping only the linear terms in $a(z, t)$, we arrive to the following

system of equations [41, 42]:

$$\frac{dP}{dz} = -\frac{c\kappa}{nv_g}\alpha_i P - \frac{c\kappa}{nv_g}\sigma_\alpha \xi P^3 - 2\gamma'' P^2, \quad (6)$$

$$\frac{d\Phi}{dz} = -\frac{\omega_0\kappa}{nv_g}\sigma_n \xi P^2 - \gamma' P, \quad (7)$$

$$\begin{aligned} \frac{\partial a}{\partial z} = & -i\frac{\beta_2}{2}\frac{\partial^2 a}{\partial t^2} - \frac{c\kappa}{2nv_g}\alpha_i a - \frac{c\kappa}{2nv_g}\sigma_\alpha \xi P^2 [a + 4e^{i\Phi_0}(\cos \Phi_0 a' + \sin \Phi_0 a'')] + i\frac{4\omega_0\kappa}{nv_g}\sigma_n \\ & \times \xi P^2 e^{i\Phi_0}(\cos \Phi_0 a' + \sin \Phi_0 a'') - \gamma'' Pa + 2i\gamma P e^{i\Phi_0}(\cos \Phi_0 a' + \sin \Phi_0 a''). \end{aligned} \quad (8)$$

Here, σ_n and σ_α quantify the influence of FCs on the linear optical properties of silicon *via* $\delta n_{fc} = \sigma_n N$ and $\alpha_{fc} = \sigma_\alpha N$, and have values of $\sigma_\alpha = 1.45 \times 10^{-21} (\lambda/\lambda_0)^2$ (in units of m^2) and $\sigma_n = \sigma (\lambda/\lambda_0)^2$ (in units of m^3), with σ being a power-dependent coefficient [28] and $\lambda_0 = 1550 \text{ nm}$ is a reference wavelength. Note that when deriving these equations we used Eq. (5). It can be seen from Eqs. (6)–(8) that the optical power P can be calculated independently of other signal parameters and, as expected, it decays due to intrinsic losses, FC absorption (FCA), and two-photon absorption (TPA). On the other hand, the variation of the global phase, Φ , is determined by the FC dispersion (FCD) and self-phase modulation (SPM) effects.

In order to simplify the noise calculations, we transform Eq. (8) to a system of ODEs. For this, we combine this equation with its complex conjugate and Fourier transform the resulting equations for the in-phase and quadrature noise components, $a'(z, t)$ and $a''(z, t)$, respectively. These calculations yield:

$$\begin{aligned} \frac{dA'}{dz} = & -\frac{\beta_2}{2}\Omega^2 A'' - \frac{c\kappa}{2nv_g}\alpha_i A' - \frac{c\kappa}{2nv_g}\sigma_\alpha \xi P^2 [A' + 4\cos \Phi_0(\cos \Phi_0 A' + \sin \Phi_0 A'')] \\ & - \frac{4\omega_0\kappa}{nv_g}\sigma_n \xi P^2 \sin \Phi_0(\cos \Phi_0 A' + \sin \Phi_0 A'') - \gamma'' P A' \\ & - 2P(\gamma' \sin \Phi_0 + \gamma'' \cos \Phi_0)(\cos \Phi_0 A' + \sin \Phi_0 A''), \end{aligned} \quad (9)$$

$$\begin{aligned} \frac{dA''}{dz} = & \frac{\beta_2}{2}\Omega^2 A' - \frac{c\kappa}{2nv_g}\alpha_i A'' - \frac{c\kappa}{2nv_g}\sigma_\alpha \xi P^2 [A'' + 4\sin \Phi_0(\cos \Phi_0 A' + \sin \Phi_0 A'')] \\ & + \frac{4\omega_0\kappa}{nv_g}\sigma_n \xi P^2 \cos \Phi_0(\cos \Phi_0 A' + \sin \Phi_0 A'') - \gamma'' P A'' \\ & + 2P(\gamma' \cos \Phi_0 - \gamma'' \sin \Phi_0)(\cos \Phi_0 A' + \sin \Phi_0 A''), \end{aligned} \quad (10)$$

where $\Omega = \omega - \omega_0$ and $A'(z, \Omega) = \mathcal{F}\{a'(z, t)\}$ and $A''(z, \Omega) = \mathcal{F}\{a''(z, t)\}$ are the Fourier transforms of the two noise components. Furthermore, a detailed comparison between the full propagation model and its linearized version was carried out for both single-channel [42] and multi-channel systems [41], the conclusion being that for practical values of the system parameters the linearized model is accurate.

2.3. Description of the Optical Properties of the Silicon Waveguides

Two types of Si waveguides are considered in our work, as illustrated in the first block of Fig. 1. Thus, one is a single-mode Si-PhW buried in SiO_2 , with uniform cross-section of height, $h = 250 \text{ nm}$, and width, $w = 900 \text{ nm}$. The other one is a Si-PhCW consisting of a line defect along the GK direction of a PhC slab waveguide with honeycomb air hole lattice with lattice constant, $a = 412 \text{ nm}$, hole radius, $r = 0.22a$, and slab thickness, $h = 0.6a$. The Si-PhCW is designed to possess both FL and SL spectral regions [41], referred to as Si-PhCW-FL and Si-PhCW-SL, respectively, so as to facilitate the study of the dependence of the system performance on the linear and nonlinear optical coefficients of the waveguide. More specifically, due to their

Table 1. The optical parameters of silicon waveguides used in numerical simulations.

Waveguide type	λ	α_i [dB cm ⁻¹]	β_2 [ps ² m ⁻¹]	γ' [W ⁻¹ m ⁻¹]	γ'' [W ⁻¹ m ⁻¹]
Si-PhW	1550	1	0.5	166.8	50.8
Si-PhCW-FL	1550	50	-3.3×10^2	750.1	228.6
Si-PhCW-SL	1524	50	-4.3×10^4	6.94×10^3	2.12×10^3

strong dependence on the GV, in the SL regime both the linear and nonlinear optical effects are significantly enhanced as compared to the FL regime. The optical coefficients of the silicon waveguides are given in Table 1, whereas t_c is set to 0.5 ns [43] in all our calculations.

3. Optical Direct-detection Receivers for High-order PSK Modulated Signals

In this section, we introduce and briefly discuss the constellation diagrams of PSK and ASK-PSK signal modulation formats as these tools play a central role in our study. To this end, we show in Fig. 2 the symbols of 2PSK and high-order PSK (4PSK, 8PSK, and 16PSK), as well as those of ASK-PSK (A2PSK and A4PSK). As can be seen in these diagrams, in the case of PSK modulation formats all symbols have the same power, whereas for A2PSK and A4PSK each of the two and four symbols are located on two different power rings.

Let us consider now how the functionality of direct-detection receivers for high-order PSK signals is implemented using Mach-Zehnder interferometers (MZIs) [34, 35], that is how to convert phase modulation into intensity modulation before the photodiode square-law detection stage. To be more specific, in Fig. 1 we schematically illustrate a phase detection scheme employing N MZIs with properly chosen phase shifts, N representing half of the number of phase states ($N = m/2$ for m PSK signals). For each MZI, the delay time is one symbol interval and the particular value of the phase shift depends on the particular PSK format.

The direct-detection process pertaining to PSK signals can be briefly summarized as follows: The received optical signal is filtered by an optical bandpass filter and subsequently passed on to

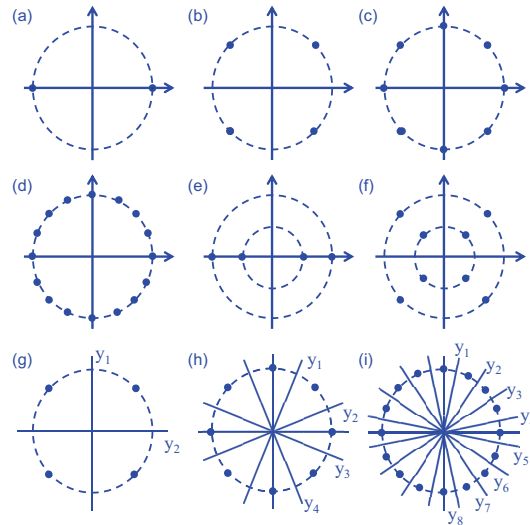


Fig. 2. Constellation diagrams of the investigated signal modulation formats. (a), (b), (c), (d), (e), (f), are for 2PSK, 4PSK, 8PSK, 16PSK, A2PSK, and A4PSK modulation, respectively. (g), (h), (i) The decision boundaries for 4PSK, 8PSK, and 16PSK modulation formats.

N MZIs, which demodulate the received PSK signal. Then, the demodulated signals pass through ideal photodiodes yielding photocurrents proportional to the difference between the intensities at the output ports of the previous MZI. Finally, these photocurrents are lowpass filtered by electrical filters. By performing bi-level electrical decisions on the resulting N photocurrents, the direct-detection process of the optical signal is completed. When applied to ASK-PSK signals, an additional branch for intensity detection must be used for a separate evaluation of the signal intensity. For example, for 4PSK and 8PSK modulation formats, two and four MZIs are needed for the direct-detection process, respectively [33, 44, 45].

4. Methods for Analysis of Direct-detection of PSK and ASK-PSK Signals

In this section we present a general formalism for the characterization of direct-detection of PSK and ASK-PSK signals with particular emphasis on BER calculations. As an illustration of the general formalism, we show how it applies to the 8PSK modulation format.

4.1. General Formalism

Our general approach to BER calculations is based on the frequency-domain KL series expansion of the transmitted signal. Importantly, the KL expansion method allows one to use much shorter pseudorandom bit sequences (PRBSs): whereas it already converges for PRBS-9, Monte-Carlo type methods could require PRBSs as long as 2^{32} to reach convergence [35].

The basic idea of KL expansion is to obtain the decision variable as a sum of uncorrelated and independent random variables *via* a set of orthonormal functions. Thus, starting from the frequency-domain signal at the output of the waveguide, $X(f)$, the decision variable for the n th port, $n = 1, \dots, N$, is expressed as a double Fourier transform:

$$y_n(t) = \int_{-\infty}^{\infty} \int_{-\infty}^{\infty} X^*(f_1) K_n(f_1, f_2) X(f_2) e^{2\pi i(f_2 - f_1)t} df_1 df_2, \quad (11)$$

where the kernel $K_n(f_1, f_2)$ is

$$K_n(f_1, f_2) = H_o^*(f_2) H_o(f_1) H_e(f_1 - f_2) [H_{n,U}^*(f_2) H_{n,U}(f_1) - H_{n,L}^*(f_2) H_{n,L}(f_1)]. \quad (12)$$

Here, $H_o(f)$, $H_e(f)$, $H_{n,U}$, and $H_{n,L}$ are the transfer functions of the bandpass optical filter, lowpass electrical filter, and the upper and lower branch of the n th MZI with the corresponding couplers included, respectively [33]. The specific forms of $H_{n,U}$ and $H_{n,L}$ depend on the type of the PSK signal. Thus, for m PSK, neglecting the phase error in MZIs, these functions are:

$$H_{n,U}(f) = \frac{1}{2} C_r \left(e^{-2\pi i f T_s} + e^{i\phi_n} \right), \quad (13)$$

$$H_{n,L}(f) = \frac{1}{2} C_r \left(e^{-2\pi i f T_s} - e^{i\phi_n} \right), \quad (14)$$

where T_s is the symbol duration, ϕ_n is the phase shift of the n th MZI, and C_r represents the coupler coefficients for m PSK and are given by $C_r = (\sqrt{2}/2)^r$, $r = \log_2 m - 1$.

The BER calculation for each MZI port is performed by using discrete Fourier transform. Thus, the frequency interval is discretized to a discrete-frequency vector with equally spaced values separated by Δf . Then, the decision variable in Eq. (11) can be written as a double sum,

$$y(t) = \sum_{\alpha=1}^{2M+1} \sum_{\beta=1}^{2M+1} x_{\alpha}^* K_{\alpha\beta} x_{\beta}, \quad (15)$$

where for convenience the port index n has been dropped and

$$x_{\alpha} = X(f_{\alpha}) e^{2\pi i f_{\alpha} t} \sqrt{\Delta f}, \quad (16)$$

$$K_{\alpha\beta} = K(f_{\alpha}, f_{\beta}) \Delta f. \quad (17)$$

Here, M is an integer chosen such that the entire relevant frequency interval is covered and $f_\alpha = (\alpha - 1 - M)\Delta f$, $\alpha = 1, \dots, 2M + 1$.

For later convenience, we now recast Eq. (15) into a real-valued equation. For this, the signal is converted to a real column vector by concatenating the real and imaginary parts of the vector, $\{x_\alpha\}$, namely $\mathbf{x} = [x' \ x'']^T$, and the kernel K is similarly converted to a $(4M + 2) \times (4M + 2)$ real matrix, $\mathcal{K} = [\hat{\mathbf{K}}' \ -\hat{\mathbf{K}}''; \hat{\mathbf{K}}'' \ \hat{\mathbf{K}}']$. As a result of these manipulations, the decision variable $y(t)$ can be expressed as:

$$y(t) = \mathbf{x}^T \cdot \mathcal{K}\mathbf{x}. \quad (18)$$

The covariance matrix associated to statistical variable \mathbf{x} , $\mathcal{R} = \mathbb{E}\{\mathbf{x}\mathbf{x}^T\}$ where $\mathbb{E}\{\cdot\}$ denotes the statistical expectation operator, can be factorized in Cholesky decomposition as $\mathcal{R} = \mathbf{\Sigma}\mathbf{\Sigma}^T$, where $\mathbf{\Sigma}$ is a lower-triangular matrix. An orthogonal matrix, $\mathbf{\Lambda}$, is then constructed so as to diagonalize the real symmetric matrix $\mathbf{\Sigma}^T\mathcal{K}\mathbf{\Sigma}$, namely:

$$\{\mathbf{\Lambda}^T\mathbf{\Sigma}^T\mathcal{K}\mathbf{\Sigma}\mathbf{\Lambda}\}_{\alpha\beta} = \eta_\alpha\delta_{\alpha\beta}, \quad (19)$$

where η_α , $\alpha = 1, \dots, 4M + 2$, are real-valued eigenvalues. If we introduce the new multivariate random variable $\mathbf{w} = \mathbf{\Lambda}^T\mathbf{\Sigma}^{-1}\mathbf{x} \equiv \mathbf{\Lambda}^T\mathbf{\Sigma}^{-1}\mathbf{s} + \mathbf{\Lambda}^T\mathbf{\Sigma}^{-1}\mathbf{n}$, where \mathbf{s} and \mathbf{n} are the signal and noise parts of \mathbf{x} , respectively, the decision variable becomes:

$$y(t) = \sum_{\alpha=1}^{4M+2} \eta_\alpha w_\alpha^2. \quad (20)$$

The statistical properties of \mathbf{w} can be easily derived from those of \mathbf{x} , as follows:

$$\mathbb{E}\{\mathbf{w}\} = \mathbf{\Lambda}^T\mathbf{\Sigma}^{-1}\mathbb{E}\{\mathbf{s} + \mathbf{n}\} = \mathbf{\Lambda}^T\mathbf{\Sigma}^{-1}\mathbb{E}\{\mathbf{s}\} \equiv \boldsymbol{\sigma}, \quad (21)$$

$$\mathbb{E}\{\mathbf{w}\mathbf{w}^T\} = \mathbb{E}\{\mathbf{\Lambda}^T\mathbf{\Sigma}^{-1}\mathbf{x}\mathbf{x}^T\mathbf{\Sigma}^{-1T}\mathbf{\Lambda}\} = \mathbf{I}, \quad (22)$$

where we have used the fact that $\mathbb{E}\{\mathbf{n}\} = 0$ and the variable $\boldsymbol{\sigma}$ is defined as $\boldsymbol{\sigma} = \mathbf{\Lambda}^T\mathbf{\Sigma}^{-1}\mathbb{E}\{\mathbf{s}\}$. These relations show that the correlation matrix of the multivariate random variable \mathbf{w} is diagonal, which means that its components are mutually uncorrelated. Using these results, the moment-generation function Ψ_y of the decision variable $y(t)$ can be written as:

$$\Psi_y(s) = \mathbb{E}\{e^{-sy}\} = \prod_{\alpha=1}^{4M+2} \frac{\exp\left(\frac{\eta_\alpha\sigma_\alpha^2 s}{\sqrt{1-2\eta_\alpha s}}\right)}{\sqrt{1-2\eta_\alpha s}}. \quad (23)$$

By using the saddle-point approximation, we can calculate the probability $\mathcal{P}(y > y_{th}|s = 0)$ [$\mathcal{P}(y < y_{th}|s = \sqrt{P})$] for an error to occur when a “0” [“1”] bit is detected. Finally, the transmission BER for the n th port can be evaluated from the following relation:

$$\mathcal{P} = \frac{1}{2} \left[\mathcal{P}(y > y_{th}|s = 0) + \mathcal{P}(y < y_{th}|s = \sqrt{P}) \right]. \quad (24)$$

4.2. Application to 8PSK Modulation Format

We now illustrate how the formalism just presented can be applied to the 8PSK modulation format. Four MZIs and bi-level electrical decision are used in an 8PSK receiver, amounting to four decision currents [39]. The Hermitian kernels $K_n(f_1, f_2)$, $n = 1, \dots, 4$, are calculated using Eqs. (13)–(14), with $n \in \{1, 2, 3, 4\}$, MZI phase shift $\phi_n \in \{3\pi/8, \pi/8, -\pi/8, -3\pi/8\}$, $C_r = 1/2$, and $T_s = 3T_0$, with T_0 being the bit window.

The decision thresholds in the signal space, which are required to decide whether an error has occurred during the signal transmission, are illustrated in Fig. 2(h). There are four decision

boundaries, labeled by $y_1, y_2, y_3,$ and y_4 , the angles of their directions being chosen to be consistent with the four MZI phase-shift values. Note that there are alternative choices for decision boundaries for 8PSK modulated signals, their advantages and disadvantages being thoroughly discussed in [45]. We also provide the threshold boundaries for 4PSK and 16PSK signals in Figs. 2(g) and 2(i), respectively, since they are important when performing the signal decoding and BER estimation. One common feature of threshold-boundary diagrams is that all decision axes coincide with constant phase lines and, in order to ensure optimum performance, are chosen in such a way that they are located at the maximum distance from adjacent symbols. This type of decision threshold is referred to “arg-decision” [34]. Finally, the overall BER is calculated by combining the BER obtained at each output port and is given by [44]:

$$BER = \frac{1 - \prod_{n=1}^4 (1 - BER_n)}{3}. \quad (25)$$

It is instructive to explore the location in signal space and eye diagrams of 8PSK signals before being converted into electrical currents. We start with the distribution of the 8PSK signals at the output of the Si waveguides and plot it in Fig. 3. In these calculations we assumed that the power is $P = 10$ mW and the length of the Si-PhW (Si-PhCW) is $L = 5$ cm ($L = 500 \mu\text{m}$). Note that in what follows we used these same values of the system parameters, unless otherwise specified. One important conclusion revealed by these calculations is that the phase spread is similar for Si-PhCW-FL and Si-PhW but is significantly smaller as compared to that of Si-PhCW-SL. On the other hand, the signal amplitude spread in the three cases has similar values. One possible explanation of this finding is that for Si γ'' is about an order of magnitude smaller than γ' , meaning that TPA has a weaker effect on the power, as compared to the extent to which SPM affects the phase. We see that even though the length of Si-PhCW is $100\times$ shorter than that of the Si-PhW, the Si-PhCW operating in the FL regime leads to much less degraded signals.

The eye diagrams of the real and imaginary part of 8PSK signals, after passing through fifth-order Butterworth optical filter, are shown in Fig. 4. The top and bottom panels represent the real and imaginary part of signals, respectively. These eye diagrams show that the amplitude decay is comparable in the Si-PhW and Si-PhCW-FL systems, but is much larger in the Si-PhCW-SL system, a fact explained by increased linear and nonlinear losses in the SL regime. Moreover, the eye opening is the smallest in the Si-PhCW-SL system when the eye diagrams are normalized so that a fair comparison can be made. This conclusion agrees with the results presented in Fig. 3.

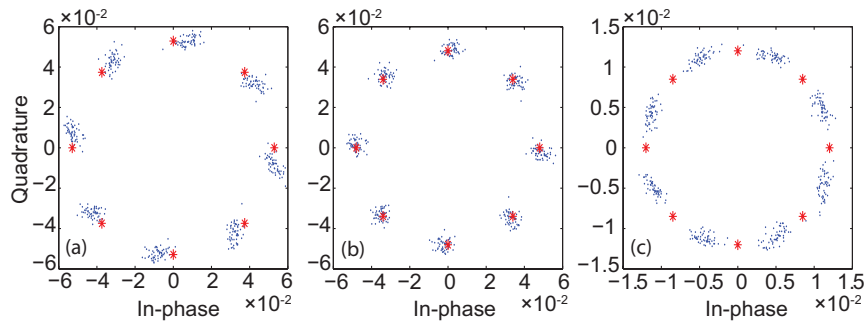


Fig. 3. (a), (b), (c) Signal constellation of 8PSK signals with $\text{SNR} = 25$ dB and $P = 10$ mW, at the output of a Si-PhW, Si-PhCW-FL, and Si-PhCW-SL, respectively. The dots indicate the noisy signals and the asterisks represent the ideal output signal without noise and phase shift.

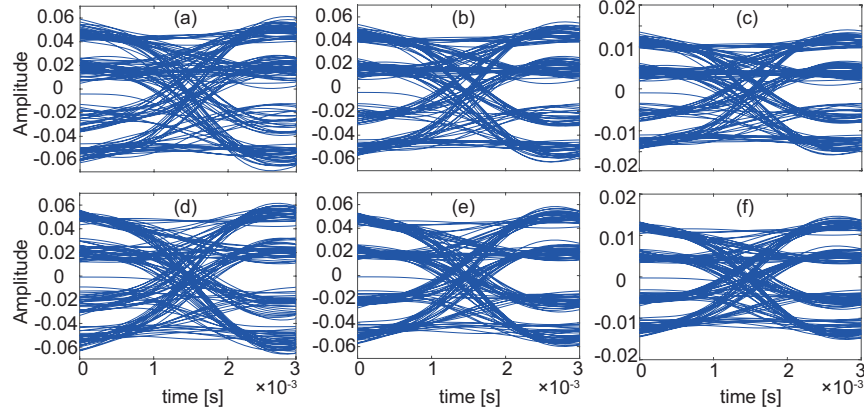


Fig. 4. Top and bottom panels show the eye diagrams of real and imaginary part of received 8PSK signals after fifth-order Butterworth optical filter, respectively. From left to right, the panels correspond to the Si-PhW, Si-PhCW-FL, and Si-PhCW-SL. The input power $P = 10$ mW, SNR = 25 dB, and length of Si-PhW and Si-PhCW is 5 cm and 500 μm , respectively.

5. Results and Discussion

We begin this section by describing the set-up of the numerical simulations. Thus, we use a PRBS of $2^9 - 1$ bits plus a zero bit, hence including all possible 9-bit sequence patterns. The bit window is $T_0 = 100$ ps and all MZIs in the direct-detection receivers have a time delay of $T_s = 3T_0$ and modulation-type related phase shifts. Note that the FC relaxation time (0.5 ns) is much shorter than the total time of the bit sequence (51.2 ns), which means that steady state is reached in our calculations. In addition, we choose low-pass integrate-and-dump electrical filters with the 3-dB bandwidth, $B_e = 10$ Gb s $^{-1}$, and bandpass Lorentzian optical filters with the 3-dB bandwidth, $B_o = 4B_e$ [42]. In order to illustrate the capabilities of our model, other types of filter configurations are considered, too.

Before presenting the main results of our analysis of the system performance, we discuss the physical conditions in which our theoretical model is valid as well as the main physical effects that influence the BER. Thus, if we assume that the signal power is $P = 5$ mW, the corresponding FC loss coefficient of the Si waveguides, α_{fc} , is 1.4×10^{-3} dB cm $^{-1}$, 1.38×10^{-2} dB cm $^{-1}$, and 1.24×10^{-1} dB cm $^{-1}$ for the Si-PhW, Si-PhCW-FL, and Si-PhCW-SL, respectively, all these values being very small compared to the intrinsic loss coefficient of the Si-PhW (1 dB cm $^{-1}$) and Si-PhCW (50 dB cm $^{-1}$). The same conclusion holds for δn_{fc} , the corresponding values being -7.91×10^{-7} , -7.73×10^{-6} , and -6.93×10^{-5} , that is well within the bounds where FC response is linear. We now turn our attention to the relative strength of dispersive and nonlinear effects. Using the values in Table 1, we find that for $P = 10$ mW and $T_0 = 100$ ps the dispersion length is $L_D = 2 \times 10^4$ m, $L_D = 30$ m, and $L_D = 0.24$ m for the Si-PhW, Si-PhCW-FL, and Si-PhCW-SL, respectively, whereas the corresponding nonlinear lengths are $L_{NL} = 1.97$ m, $L_{NL} = 0.13$ m, and $L_{NL} = 0.014$ m. This shows that nonlinearity plays a much more important role than the waveguide dispersion in defining the optical signal dynamics.

The BER for all modulation formats was simulated for different values of the signal-to-noise ratio (SNR), for the Si-PhW, Si-PhCW-FL, and Si-PhCW-SL systems depicted in Fig. 1, the results being summarized in Fig. 5. A first conclusion of these numerical investigations is that the system BER increases as the order of PSK signal increases. In particular, ranked from the highest to lowest BER, the modulation formats are 16PSK, 8PSK, A4PSK, A2PSK, 4PSK, and 2PSK. Note that in the case of A4PSK and A2PSK signals, the power in the outer circle was chosen to

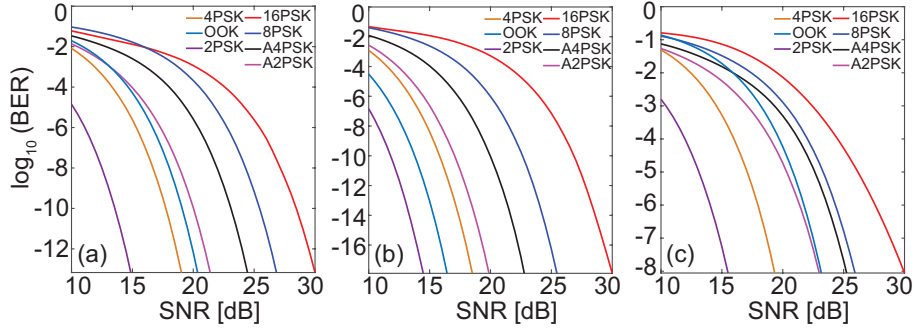


Fig. 5. System BER of various modulation formats for direct-detection receivers with bi-level decision. From left to right, the panels correspond to a Si-PhW, a Si-PhCW operated in the FL regime, and a Si-PhCW operated in the SL regime.

be twice as large as that in the inner one and since we set the average power to be the same in all simulations, the power of OOK for bit “1” is twice as large as the average power. Moreover, these power considerations make it easy to understand why OOK and PSK signals have different signal quality after detection, namely because the average not the peak optical power is the power parameter directly related to the transmission BER [42].

Another significant idea revealed by the plots in Fig. 5 is that, for all types of PSK signals, the Si-PhCW-SL system shows the worst performance. This result implies that the advantages associated to SL operation, namely enhanced nonlinear optical interactions and consequently reduced device footprint, could be outweighed by poor BER. On the other hand, the best BER performance is achieved using the same Si-PhCW but when operated in the FL regime, as per Fig. 5(b). This clearly underlines the importance of the interplay between the favorable role played by enhanced dispersive and nonlinear effects in the SL regime in reducing the device size and their detrimental influence on transmission BER.

A key parameter on which the performance of optical communication systems depends is the signal power. In the case of Si optical interconnects with subwavelength cross-section this influence is particularly critical due to tight light confinement and SL effects. Therefore, we have investigated the dependence of transmission BER on the input power and its relationship with the type of signal modulation format. To illustrate the main findings of this analysis, we show in Fig. 6 the variation of BER with the SNR for A2PSK, 4PSK, and 2PSK signals, determined for different values of the input power.

As expected, this figure shows that BER increases with the optical power, irrespective of the signal format. We can also see that the Si-PhCW-FL system is characterized by the weakest dependence of BER on power, chiefly because only a small nonlinear phase accumulates over the short length of this waveguide. In addition, as the signal propagates over a short distance, the FC phase-shift is small, too. These results agree with the data plotted in Fig. 3(b), which shows that indeed the smallest phase-shift corresponds to the Si-PhCW-FL system. By contrast, the phase variations at the output of the Si waveguides are the largest when the PhC waveguide is operated in the SL regime, which in this case is reflected in a strong power dependence of the BER. As a conclusion to this discussion, the Si-PhCW operated in the FL regime represents the optimum choice for on-chip Si optical interconnects, due to the best transmission BER and its relatively small dimensions. Importantly, however, all three systems are suitable for chip-level optical communication networks using PSK modulation formats, as for properly chosen SNR the BER is below a quasi-error free level, e.g. $BER < 10^{-9}$.

The results presented so far show that the transmission BER depends not only on the optical power and type of signal modulation format but also on the waveguide length. In order to further

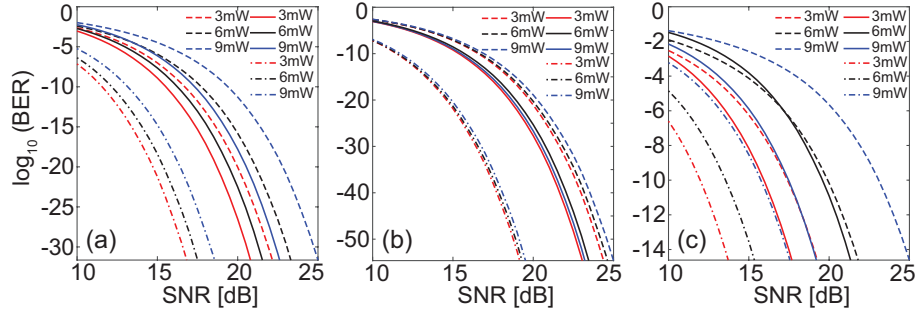


Fig. 6. System BER vs. SNR determined for different input power. From left to right, the panels correspond to a Si-PhW, a Si-PhCW operated in the FL regime, and Si-PhCW operated in the SL regime. The dashed lines, solid lines and dash-dot lines correspond to A2PSK, 4PSK, and 2PSK modulated signals, respectively.

clarify this length dependence of BER, we varied the length of the two types of waveguides but kept constant and equal to 100 the ratio between the lengths of the Si-PhW and Si-PhCW. The corresponding BER curves, calculated for A2PSK, 4PSK, and 2PSK signals and $P = 10$ mW, are depicted in Fig. 7. As expected, in all cases investigated, the signal impairments increase as the waveguide length increases, this variation being the steepest in the case of Si-PhCW-SL systems. If on the other hand we compare the system performance corresponding to the three modulation formats, one concludes that the strongest dependence of BER on the waveguide length is observed in the case of 2PSK signal, the overall system performance being the worst in this case, too. In addition, it can be seen in Fig. 7 that the Si-PhCW-FL system shows weakest length dependence of BER, which again is consistent with the results presented in Fig. 6(b).

For completeness, we also studied the extent to which the transmission BER depends on the system configuration, namely the type of optical and electrical filters used. In this analysis, we considered an 8PSK signal modulation and calculated the dependence of BER on SNR for the three waveguide systems, namely Si-PhW, Si-PhCW-FL, and Si-PhCW-SL, for different types of filters. More specifically, the electrical filter was a fifth-order Bessel filter with bandwidth of 10 Gb s^{-1} , whereas the optical filters were a Lorentzian filter, Gaussian filter, super-Gaussian filter, and sixth-order Butterworth filters, all with bandwidth of 40 Gb s^{-1} . The results of these

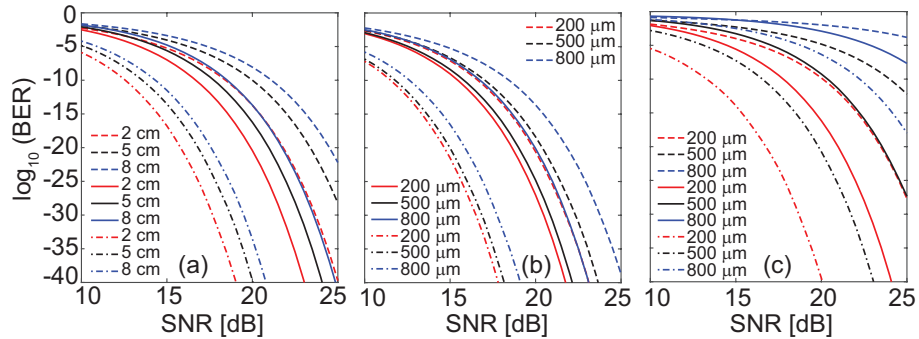


Fig. 7. System BER vs SNR, calculated for different waveguide lengths. From left to right, the panels correspond to a Si-PhW, a Si-PhCW operated in the FL regime, and Si-PhCW operated in the SL regime. The dashed lines, solid lines, and dash-dot lines correspond to A2PSK, 4PSK, and 2PSK modulated signals, respectively.

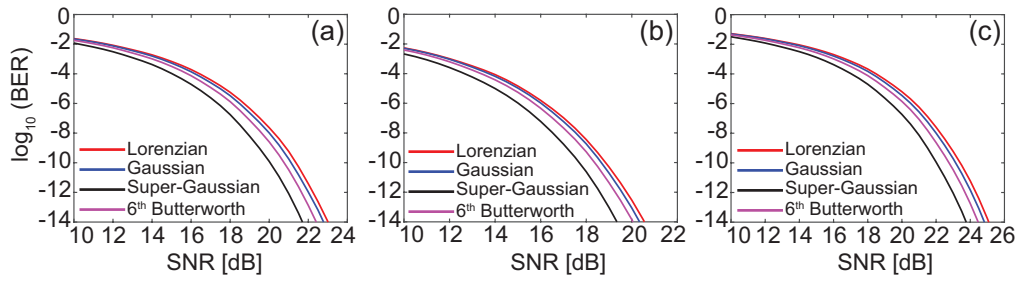


Fig. 8. BER calculated for several system receiver configurations. From left to right, the panels correspond to a Si-PhW, a Si-PhCW operated in the FL regime, and Si-PhCW operated in the SL regime. In all cases, an 8PSK modulation format is considered. The electrical filter is a fifth-order Bessel filter, whereas the optical filter is a Lorenzen filter (red line), Gaussian filter (blue line), super-Gaussian filter (black line), and sixth-order Butterworth filter (purple line).

calculations are summarized in Fig. 8. The main conclusion of these investigations is that, in all cases, the optimum choice is the super-Gaussian filter, whereas the worst performance corresponds to the Lorenzian one. The variation of the system performance with the type of filter, however, is relatively small for all waveguides considered.

6. Conclusion

In conclusion, we have presented a comprehensive theoretical and computational analysis of the performance of photonic systems containing silicon based optical interconnects and employing high-order phase-shift keying modulation formats. The systems consisted of optical waveguides made of silicon and direct-detection receivers. The silicon optical interconnects were designed so as to possess fast- and slow-light propagation regimes, which allowed us to investigate the relationships between the system performance and the linear and nonlinear optical coefficients of the optical waveguides. Importantly, by considering different types of phase-shift keying modulation formats, we have identified those most suitable to be used in photonic systems containing silicon based optical interconnects. In addition, using the theoretical models and computational methods introduced in this study we have investigated the dependence of the performance of systems employing high-order modulation formats on the optical properties of silicon interconnects and signal characteristics. In particular, this analysis has revealed that the higher the order of the signal modulation format is, the worse the bit-error ratio is.

7. Funding

China Scholarship Council (CSC); European Research Council (ERC) (ERC-2014-CoG-648328).